An agent-based modeling approach for lung fibrosis in response to COVID-19

Mohammad Aminul Islam[1], Michael Getz[2], Paul Macklin[2], Ashlee N. Ford Versypt[1,3,4*]

1 Department of Chemical and Biological Engineering, University at Buffalo, The State University of New York, Buffalo, NY, 14260, USA
2 Department of Intelligent Systems Engineering, Indiana University, Bloomington, IN, 47408, USA
3Department of Biomedical Engineering, University at Buffalo, The State University of New York, Buffalo, NY 14260, USA
4Institute for Artificial Intelligence and Data Science, University at Buffalo, The State University of New York, Buffalo, NY 14260, USA

* ashleefv@buffalo.edu

Abstract

The severity of the COVID-19 pandemic has created an emerging need to investigate the long-term effects of infection on patients. Many individuals are at risk of suffering pulmonary fibrosis due to the pathogenesis of lung injury and impairment in the healing mechanism. Fibroblasts are the central mediators of extracellular matrix (ECM) deposition during tissue regeneration, regulated by anti-inflammatory cytokines including transforming growth factor beta (TGF-β). The TGF-β-dependent accumulation of fibroblasts at the damaged site and excess fibrillar collagen deposition lead to fibrosis. We developed an open-source, multiscale tissue simulator to investigate the role of TGF-β sources in the progression of lung fibrosis after SARS-CoV-2 exposure, intracellular viral replication, infection of epithelial cells, and host immune response. Using the model, we predicted the dynamics of fibroblasts, TGF-β, and collagen deposition for 15 days post-infection in virtual lung tissue. Our results showed variation in collagen area fractions between 2% and 40% depending on the spatial behavior of the sources (stationary or mobile), the rate of activation of TGF-β, and the duration of TGF-β sources. We identified M2 macrophages as primary contributors to higher collagen area fraction. Our simulation results also predicted fibrotic outcomes even with lower collagen area fraction when spatially-localized latent TGF-β sources were active for longer times. Our results showed that partial removal of TGF-β sources changed the fibrotic patterns; in the presence of persistent TGF-β sources, partial removal of TGF-β from the ECM significantly increased collagen area fraction due to maintenance of chemotactic gradients driving fibroblast movement. The computational findings are consistent with independent experimental and clinical observations of collagen area fractions and cell population dynamics not used in developing the model. These critical insights into the activity of TGF-β sources may find applications in the current clinical trials targeting TGF-β for the resolution of lung fibrosis.

Author summary

COVID-19 survivors are at risk of lung fibrosis as a long-term effect. Lung fibrosis is the excess deposition of tissue materials in the lung that hinder gas exchange and can

collapse the whole organ. We identified TGF-β as a critical regulator of fibrosis. We built a model to investigate the mechanisms of TGF-β sources in the process of fibrosis. Our results showed spatial behavior of sources (stationary or mobile) and their activity (activation rate of TGF-β, longer activation of sources) could lead to lung fibrosis. Current clinical trials for fibrosis that target TGF-β need to consider TGF-β sources' spatial properties and activity to develop better treatment strategies.

Introduction

Severe acute respiratory syndrome coronavirus 2 (SARS-CoV-2) is responsible for the coronavirus disease 19 (COVID-19) pandemic and primarily causes pulmonary infection with symptoms and complications ranging from short-term pneumonia to long-term acute respiratory distress syndrome (ARDS) [1–3]. The long-term respiratory complications of COVID-19 survivors include diffuse alveolar damage (DAD), which is also a histological hallmark of ARDS [4]. DAD begins with the exudative phase when edema and inflammation occur, followed by the fibroproliferative phase with loose-organizing fibrosis. In the fibroproliferative phase, damaged tissues are partially replaced through fibroblast migration, proliferation, and collagen deposition. But impairments in the repair mechanisms—such as persistent infections [5], imbalances between profibrotic and antifibrotic mediators [6], and dysregulation in the functions of immune cells [7, 8] and fibroblasts [9, 10]—can lead to long-term fibrosis.

The severity of SARS-CoV-2 infection dictates the severity of pulmonary fibrosis. Zou et al. [11] reported that 100% of patients with severe and critical COVID-19 disease generate pulmonary fibrosis, wherein severe fibrosis is observed in most cases. Although 90-day follow-up results in their studies showed significant resolution in most patients, some patients had fibrotic areas after 90 days. In another study, Li et al. [2] reported that 59.6% of patients with confirmed COVID-19 cases had lung fibrosis after 90 days from onset. The overall lung fibrosis in hospitalized patients was 86.87%, out of which only 31.74% of patients had eventual resolution of fibrosis in follow-up visits. The six-month follow-up computed tomography scan of severe COVID-19 pneumonia survivors in the study of Han et al. [12] showed fibrotic changes in 35% of patients. They identified that susceptible groups have ARDS, higher heart rates, older age, longer hospital stays, and noninvasive mechanical ventilation. COVID-19 pulmonary fibrosis is different from other fibrotic lung diseases, e.g., idiopathic pulmonary fibrosis (IPF), as injuries occur at the site of epithelial cells rather than endothelial cells [3]. Currently, the mechanistic basis for progressive and stable fibrosis resolution is not completely understood.

Macrophages play an essential role in different phases of DAD. Inflammatory macrophages (M1 macrophages) are activated during the exudative phase of tissue damage to provide host defense [13]. At the same time, M1 macrophages are responsible for inflammation and lung injury. In the fibroproliferative phase of DAD, M1 macrophages shift to alternatively activated macrophages (M2 macrophages) and start secreting anti-inflammatory cytokines (e.g., TGF-β), clearing apoptotic cells, and removing debris [14]. M2 macrophages play a crucial role in developing and resolving tissue damage in the fibroproliferative and fibrotic stages of DAD [15, 16].

Another critical contributor to fibrosis is the activation of latent TGF-β due to tissue damage. TGF-β is always secreted in a latent form that must be activated. Depending on the spatial behavior of the sources of TGF-β, they can be categorized into two groups: stationary sources (e.g., latent stores of TGF-β) and mobile sources (e.g., M2 macrophages). Excess TGF-β that is not activated within a short time of synthesis is stored in extracellular matrix (ECM) as latent deposits that are spatially restricted [17]. Latent TGF-β is stored at high concentrations in the ECM in an inactive state in most

organs, including the lung [18]. Injury and death of epithelial cells due to external stimuli activate the latent TGF-β in the ECM at the damaged sites using αvβ6 integrins [9,19]. Latent TGF-β can also be activated by reactive oxygen species, low pH, and proteolysis [20] and from cell surfaces [21]. Here, we refer to activation of TGF-β from the ECM stores without *de novo* synthesis as "stationary sources" of TGF-β.

Other sources of TGF-β in pulmonary fibrosis are M2 macrophages, metaplastic type II alveolar epithelial cells (AECs), bronchial epithelium, eosinophils, fibroblasts, and myofibroblasts [20,22]. In this work, *de novo* synthesis of latent TGF-β from anti-inflammatory M2 macrophages after clearance of dead epithelial cell debris [23] is assumed to be immediately activated; thus, this source of TGF-β is considered to be "mobile". This is intended to capture the activation of latent TGF-β from cell surfaces including M2 macrophages [21,24,25].

Overexpression of TGF-β from any source and the persistent presence of any source can lead to fibrosis. Experimental observations in rat models showed the progression of pulmonary fibrosis with overexpression of TGF-β [26]. Also, quantification of TGF-β in the plasma of COVID-19 patients showed an increase in TGF-β concentration compared to healthy individuals [27,28].

Activated TGF-β directs the functions of fibroblasts. Resident fibroblasts are located beneath epithelial cells or scattered in the ECM between the lung's epithelial and endothelial layers [29]. The accumulation of TGF-β due to viral infection and epithelial cell injury recruits fibroblasts [30]. Small injuries can be repaired by the proliferation and differentiation of type 2 AECs to type 1 AECs. In contrast, the restoration process fails in severe injuries, leading to fibroblast activation and fibrosis [9]. Activated fibroblasts continually secrete ECM (e.g., collagen) to maintain the structural integrity of the lung [31]. TGF-β also regulates the collagen deposition rate of fibroblasts [32].

The current identification methods of lung fibrosis include histologic analysis of tissue samples and radiographic examination with computed tomography [33,34]. Fibrotic pattern, collagen area fraction, and localization of cells can be observed from the histological analysis. Collagen area fractions evaluated from histopathological images are strongly correlated with histologic fibrosis scores and provide a reliable index to quantify fibrosis [35].

Existing mathematical and computational models can give insights into the fundamental processes that regulate fibrotic outcomes. Brown et al. [36] developed a simple agent-based model (ABM) considering the effects of the pro-inflammatory mediator TNF-α in lung tissue damage and the anti-inflammatory mediator TGF-β1 in fibroblast-mediated collagen deposition due to exposure to smoke particles. Their model captured the histological observation of self-resolving tissue damage, localized tissue damage with fibrosis, and extensive tissue damage with fibrotic states. The ABM of Warsinske et al. [37] explored the co-regulatory relationship between epithelial cells and fibroblasts through TGF-β1 during fibrosis. In another 3D ABM of lung fibrosis [38], the initial amount of damaged type 2 AECs activated the inactive TGF-β. The ABM of Ceresa et al. [39] focused on emphysema progression (excess degradation of collagen) in chronic obstructive pulmonary disease and considered the transition of macrophages between the M1 and M2 phenotypes, secretion of TGF-β from M2 macrophages, recruitment of fibroblasts by TGF-β, fibroblast-mediated collagen deposition, and collagen degradation by MMP9. The mathematical model of Hao et al. [40] used continuous partial differential equations for IPF and considered crucial cells and cytokines for the fibrosis process, including the transition of M1 macrophages to the M2 phenotype and TGF-β-mediated fibroblast proliferation. Their results showed how treatments that block the activity of cytokines (e.g., anti-TGF-β) could reduce the excess formation of ECM. While fibrosis in the lung and other organs such as the heart differ in etiology and outcome, many important similarities exist at the cellular and

chemical levels between cardiac and pulmonary fibrosis [41]. Cardiac fibrosis is an area with rich experimental data and computational modeling studies. One study combined experiments and mathematical modeling to investigate the role of TGF-β in fibroblast-mediated collagen deposition during myocardial infarction (MI) [42]. Chowkwale et al. [43] also investigated inflammation-fibrosis coupling during MI considering the activation of latent TGF-β and TGF-β-dependent proliferation of fibroblasts. The coupled ABM and logic-based model of Rikard et al. [44] simulated similar increases in collagen area fractions to experimental observations during MI. Their model also considered the generation of latent TGF-β and fibroblast-mediated collagen deposition. In summary, TGF-β and fibroblasts are standard players in fibrosis progression in all the models described above, and major sources of TGF-β are M2 macrophages and latent stores of TGF-β. Although none of the models considered fibrosis due to viral infection, the process of fibrosis due to SARS-CoV-2 infection involves similar cells and chemical mediators.

We developed a multiscale lung tissue simulator that can be used to investigate the mechanisms of intracellular viral replication, infection of epithelial cells, host immune response, and tissue damage [45]. Here, we focused on the mechanisms of the fibrotic process in the lung tissue during SARS-CoV-2 infection. We conducted *in silico* experiments to determine the effects of the spatial behavior of TGF-β sources (stationary and mobile), the activation rate of TGF-β from sources, and the activation duration of TGF-β sources in the development and progression of fibrosis. We used collagen area fractions from histological analysis to compare the outcomes of our model simulations.

Methods

Overall model

In our earlier work, we developed a SARS-CoV-2 lung tissue simulator [45], which we refer to as the "overall model". Here, we briefly recap the most salient features of this overall model before describing our new contribution: the fibrosis model. The overall model structure is developed in an open-source multiscale ABM framework PhysiCell [46] and simulates a tissue section of $800\,\mu m \times 800\,\mu m \times 20\,\mu m$, representing a monolayer of stationary epithelial cells on an alveolar surface of lung tissue. Initially, 2793 epithelial cells, 50 resident macrophages, 28 dendritic cells, and 57 fibroblasts are present in the simulated tissue. These initializations are directly from the code used in our earlier manuscript [45]; here, we maintain the same cellular initializations. Cells are recruited to tissue through voxels that represent vasculature points; we randomly assign 8.8% voxels as vasculature points for arrivals of recruited cells because approximately this percentage of the tissue consists of the vasculature [47]. Cellular movement and diffusion of substrates occur along a 2D plane through or above the tissue, represented by a single layer of 3D voxels; this is consistent with the transport through thin alveolar tissue. We infect the simulated tissue by placing SARS-CoV-2 viral particles in the extracellular space using a uniform random distribution. Viral particles diffuse through tissue, bind with unoccupied ACE2 receptors on the epithelial cell surfaces, internalize via endocytosis, replicate through intracellular viral replication kinetics, and export back to the extracellular domain by exocytosis. Details of the intracellular virus model for replication kinetics, viral response, and receptor trafficking are described in much greater detail in our earlier manuscript [45]. After the infection, innate and adaptive immune cells become activated. In the early phase of infection, innate immune cells—macrophages, neutrophils, and dendritic cells—are recruited and are subsequently activated in the presence of viral particles and infected cells. We consider five states of

macrophages: inactivated, M1 phenotype, M2 phenotype, hyperactive, and exhausted. Both M1 and M2 phenotypes can also exist in hyperactive and exhausted states. Infected cells and M1 macrophages secrete pro-inflammatory cytokines that recruit other immune cells. Macrophages and neutrophils move along the gradient of debris from dead cells, phagocytose dead cells, and clear viral particles. Dendritic cells emigrate to the lymph node and recruit CD4+ T cells and CD8+ T cells. CD8+ T cells kill infected cells. Immune cells move along the gradient of chemokines secreted from infected cells. Further details of the immune and lymph node models are available elsewhere [45, 48].

Fibrosis model

We extended the overall model to include the mechanisms for fibrosis (Fig 1). We used the ABM platform PhysiCell to simulate the rules for phenotypic and chemical changes, including cell cycle, volume changes, death processes, cellular movement, and recruitment of the agents in Fig 1, in addition to the other processes included in the overall model. The rules for the following cell types in the fibrosis model (Fig 1)—epithelial cells, infected cells, CD8+ T cells, and M1 macrophages—are all used directly from the overall model [45].

Several additional processes are included in the fibrosis model. These involve the secreting agents, M2 macrophages, inactive and activated fibroblasts, TGF-β, and collagen. The death of an infected epithelial cell (I in Fig 1) activates the latent TGF-β embedded in the tissue ECM. The activation of latent stores of TGF-β is represented by creating a stationary secreting agent (S in Fig 1) at the site and time of epithelial cell death. The secreting agents secrete TGF-β for a certain period as the amount of TGF-β stored in the ECM is limited; a death rate of secreting agents (AT) is used to represent terminating the activation of latent stores of TGF-β. Here, death rate AT is analogous to the extinction rate of the ECM-bound TGF-β sources and is inversely proportional to the mean duration of those sources.

Macrophages are the mobile sources of TGF-β in this fibrosis model. M1 macrophages are recruited in the initial phase, and CD8+ T cells are recruited in the later stage of infection. Usually, regulatory T cells (Tregs), a subset of CD4+ T cells, are involved in the phenotypic transformation of M1 to M2 macrophages [14]. Although we do not have Tregs in the current model, CD8+ T cells exhibit similar behavior by inhibiting the secretion of pro-inflammatory cytokines from M1 macrophages in the later phase of infection [45]. Since the fibroproliferative phase of DAD occurs in the later phase of the disease, a conditional rule is added in the fibrosis model to follow this pathology: if a CD8+ T cell and an M1 macrophage are within close proximity, then the M1 macrophage stops secreting pro-inflammatory cytokines, transforms to an M2 macrophage, and starts secreting TGF-β. The interaction distance for this transition is calculated using a multiple (ϵ) of the radii of the two interacting immune cells [45]. The transformation of the M1 to M2 phenotype is considered to occur instantaneously when the distance between an M1 macrophage and a CD8+ T cell is $\leq \epsilon$ multiplied by the sum of the radii of the M1 macrophage and the CD8+ T cell. The cell radii are computed in PhysiCell as cell volumes are over updated time as the cell cycle progresses. The initial volume of macrophages is 4849 μm^3 and that for CD8+ T cell is 478 μm^3 with nuclear volumes of 10% of the cell volumes; these are the same values specified in the overall model [49].

PhysiCell is coupled to BioFVM [50], which solves partial differential equations for chemicals considered to be continuous (as opposed to the discrete agents) with terms for diffusion, decay, uptake, and release of multiple substances simultaneously. We simulate

extracellular concentrations of TGF-β (T_β) using the standard BioFVM formulation:

$$\frac{\partial T_\beta}{\partial t} = D_{T\beta}\nabla^2 T_\beta - \mu_{T\beta} T_\beta + \sum_{cells\ i} \delta(x - x_i) E_{T\beta,i} \tag{1}$$

where t is time, $D_{T\beta}$ is the diffusion coefficient of TGF-β, $\mu_{T\beta}$ is the net decay and bulk removal rate, $\delta(x)$ is the discrete Dirac delta function, x is the center of the voxel, x_i is the position of the center of discrete cell i, and $E_{T\beta,i}$ is the net export rate of TGF-β from cell i. Net export rate $E_{T\beta,i}$ denotes activation rate of latent stores of TGF-β at the damaged site, which we term damaged-site secretion (DS), or TGF-β secretion and activation rate from macrophages, which we term macrophage secretion (MS).

TGF-β activates the resident inactive fibroblasts. We assume that inactive fibroblasts become active fibroblasts in the presence of TGF-β ($T_\beta > 0$) and switch back to the inactive state in the absence of TGF-β ($T_\beta = 0$). The active fibroblasts undergo apoptosis naturally at a rate of μ_F and become dead cells. The inactive fibroblasts do not undergo apoptosis (i.e., $\mu_F = 0$) and move randomly throughout the domain. Both inactive and active fibroblasts are subject to the cycle cell model in PhysiCell where their cell volumes are over updated time as the cell cycle progresses. The initial volume of a fibroblast (F_V) and the corresponding nucleus (F_{VN}) are specified.

The activated fibroblasts chemotax up the gradient of TGF-β. The chemotaxis velocity of a fibroblast ($\vec{v}_{mot}$) depends on the TGF-β concentration in its neighboring regions, fibroblast speed (s_{mot}), migration bias (b), and time for persistence in a specific trajectory (Δt_{mot}) [45]:

$$\vec{v}_{mot} = s_{mot} \frac{b\vec{b} + (1-b)\vec{\xi}}{\left\| b\vec{b} + (1-b)\vec{\xi} \right\|} \tag{2}$$

where s_{mot} is the speed of chemotaxis, $0 \leq b \leq 1$ is the level of migration bias (i.e., $b = 0$ represents no influence of chemotaxis and only random cell migration), $\vec{\xi}$ is a random unit vector direction, and $\vec{b}$ is the migration bias direction. Fibroblasts also persist on their given trajectory for Δt_{mot} before a new trajectory is computed. For fibroblasts, $\vec{b}$ is estimated from the gradient of TGF-β concentrations in the neighboring regions [45]:

$$\vec{b} = \frac{\nabla T_\beta}{\|\nabla T_\beta\|} \tag{3}$$

New fibroblasts are recruited into the tissue by TGF-β. The number of fibroblasts recruited to the tissue (N_r) is determined by integrating the recruitment signal over the whole domain:

$$N_r = r_r \int_\Omega \min\left(1, \max\left(0, \frac{s_{cytokine} - s_{min}}{s_{sat} - s_{min}}\right)\right) dV \Delta t_r \tag{4}$$

where Ω is the computational domain, r_r is the recruitment rate (per volume), s_{min} is the minimum recruitment signal, s_{sat} is the saturating or maximum signal, and $s_{cytokine}$ is the recruitment signal that depends on the cytokine concentration. Recruitment of any immune cell by a specific cytokine in the overall model follows this formulation; proinflammatory cytokine-dependent recruitment of CD8+ T cells and macrophages is already included in the overall model [45]. The volume of each grid voxel is $dV = 20 \times 20 \times 20\,\mu\text{m}^3$, and the time interval for recruitment of fibroblasts is $\Delta t_r = 10$ min, the same as in the overall model [45]. Eq 4 gives the number of fibroblasts recruited between t and $t + \Delta t_r$. Here, $s_{cytokine} = F_g(T_\beta)$ for the recruitment signal of fibroblasts via the cytokine TGF-β.

The function for TGF-β-dependent recruitment of fibroblasts ($F_g(T_\beta)$)—particularly its specific parameters—comes from previously published works [39, 42] and is illustrated

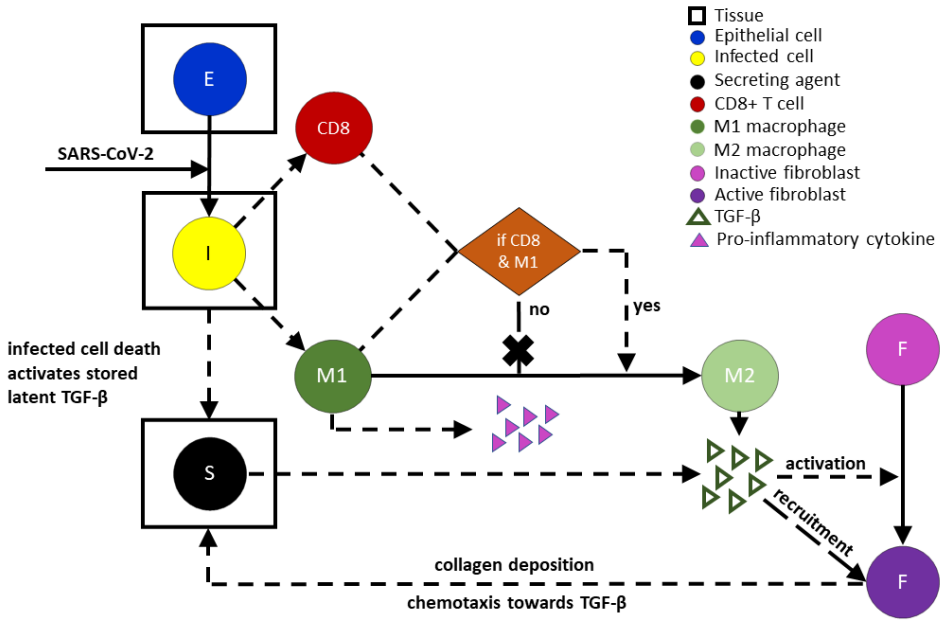

Fig 1. Cellular and chemical mediators in lung fibrosis during SARS-CoV-2 infection included in the fibrosis model. Secreting agents (S) mimic the activation of latent stores of TGF-β by acting as stationary sources of TGF-β for a certain period at the site and time of death of infected epithelial cells (I). Infected cells recruit M1 macrophages initially as an innate immune response and CD8+ T cells in the later phase of infection as an adaptive immune response. M1 macrophages stop secreting pro-inflammatory cytokines when located within close proximity to CD8+ T cells and instantaneously convert to M2 macrophages. M2 macrophages secrete and activate TGF-β and are considered mobile sources. Fibroblasts become activated and recruited by TGF-β, chemotax towards the gradient of TGF-β, and deposit collagen continuously. Cells with rectangles drawn around them represent stationary cells in tissue sections, while all other cells are considered to be mobile cells. Solid arrows denote the transformation of one cell species to another, dotted lines denote interactions that influence processes without the source being produced or consumed, and the X over an arrow indicates the process does not occur. Triangles represent secreted chemical factors that can diffuse and interact in the system.

in Fig S1A. We use a threshold value of TGF-β concentration beyond which $F_g(T_\beta)$ is assumed to be constant because of the polynomial nature of the recruitment signal.

$$F_g(T_\beta) = \begin{cases} 0.0492T_\beta^3 - 0.9868T_\beta^2 + 6.5408T_\beta + 7.1092, & \text{if } 0 < T_\beta \leq 10 \\ 22.928, & \text{else if } T_\beta > 10 \\ 0, & \text{otherwise} \end{cases} \tag{5}$$

The activated fibroblasts deposit collagen continuously. The newly deposited collagen is assumed to not diffuse or degrade. TGF-β-dependent collagen deposition from fibroblasts is described by

$$\frac{\partial C}{\partial t} = \sum_{cells\ i} \delta(x - x_i) E_{C,i} \tag{6}$$

and

$$E_{C,i} = k_{FC} F_c(T_\beta) = k_{FC} \frac{V_{T\beta} T_\beta}{k_{T\beta} + T_\beta} \tag{7}$$

where C in the concentration of collagen, $E_{C,i}$ is the net export rate of collagen from fibroblast cell i, and k_{FC} is the collagen production rate by fibroblasts. $F_c(T_\beta)$ defines the TGF-β dependence of fibroblast-mediated collagen deposition (Fig S1B), which is assumed to follow a Michaelis-Menten form, where $V_{T\beta}$ and $k_{T\beta}$ are the Michaelis-Menten limiting rate and half saturation parameters, respectively.

Parameter estimation

Experimental data from the literature used in this section were extracted from graphs in the original sources (referenced in the text) using the open-source Java program Plot Digitizer [51]. The initial values of the species in the uninfected condition are listed in Table 1. The estimated and calculated parameters are listed in Table 2. Several parameters were taken from the literature without new parameter estimation: AT, ϵ, $D_{T\beta}$, $\mu_{T\beta}$, μ_F, F_V, F_{VN}, V_F, s_{mot}, b, Δt_{mot}, and r_r. Their values and sources are also listed in Table 2. AT was also varied in one of the *in silico* experiments.

Table 1. Initial conditions for model variables

Symbol	Definition	Initial condition
F_0	Initial number of fibroblasts	57 cells [52]
C_0	Initial concentration of collagen	0 μg μm^{-3}
$T_{\beta,0}$	Initial concentration of TGF-β	0 ng mL^{-1}

The initial number of fibroblasts (F_0) was selected based on *in vivo* experiments of mice models of MI [52]. We extracted the fibroblast population per surface area from the experimental control condition and multiplied it by the surface area of the computational domain ($800 \times 800\,\mu m^2$) to evaluate the initial number of inactive resident fibroblasts in the simulated tissue. No fibroblasts are activate at $t = 0$. We considered the concentrations of TGF-β (T_β) and collagen deposited (C) to be changes from homeostatic values and set them to 0 as initial values (Table 1).

We evaluated the signal of TGF-β to recruit new fibroblasts ($s_{cytokine}$) in Eq 4 using TGF-β-dependent recruitment of fibroblasts rate from Eq 5 (Fig S1A), i.e., $s_{cytokine} = F_g(T_\beta)$. The minimum and maximum (i.e., saturating) recruitment signals (s_{min} and s_{sat}, respectively) were calculated using Eq 5 for the lower (0 ng/mL) and upper (10 ng/mL) ranges of TGF-β, respectively.

Table 2. Parameters for the fibrosis model

Symbol	Definition	Value	Unit	Source
AT	Secreting agent death rate	1×10^{-3}	min^{-1}	estimated from [42]
ϵ	Multiple of interaction distance for immune cells	1.75	Unitless	[45]
$D_{T\beta}$	TGF-β diffusion coefficient	3000	μm^2 min^{-1}	[40]
$\mu_{T\beta}$	TGF-β degradation rate	15	day^{-1}	[39]
DS	TGF-β activation rate from a damaged site	5×10^{-10}–2×10^{-9}	ng min^{-1}	estimated
MS	TGF-β secretion rate from an M2 macrophage	5×10^{-10}–5×10^{-9}	ng min^{-1}	estimated
μ_F	Active fibroblast apoptosis rate	8.30×10^{-5}	min^{-1}	[39]
F_V	Fibroblast cell volume	2500	μm^3	[53]
F_{VN}	Fibroblast nucleus volume	500	μm^3	[54]
V_F	Fibroblast velocity	1	μm min^{-1}	[55]
s_{mot}	Fibroblast speed	1	μm min^{-1}	[55]
b	Fibroblast migration bias	0.7	Unitless	[45]
Δt_{mot}	Fibroblast directional persistence	5	min	[49]
r_r	Fibroblast recruitment rate	4×10^{-9}	cells μm^{-3} min^{-1}	[45]
s_{min}	Minimum fibroblast recruitment signal of TGF-β	7.1092	ng mL^{-1}	calculated by Eq 5
s_{sat}	Maximum/saturating fibroblast recruitment signal of TGF-β	22.928	ng mL^{-1}	calculated by Eq 5
k_{FC}	Fibroblast collagen production rate	2.52×10^{-7}	μg min^{-1}	estimated from [40]
$V_{T\beta}$	Rate parameter for TGF-β-dependent collagen deposition	9.42×10^{-1}	Unitless	estimated from [56, 57] data
$k_{T\beta}$	Saturation parameter for TGF-β-dependent collagen deposition	1.74×10^{-1}	Unitless	estimated from [56, 57] data
U_F	Uptake rate of TGF-β by each fibroblast	1×10^{-1}	min^{-1}	estimated

The fibroblast collagen production rate (k_{FC}) was estimated from Hao et al. [40] (details in the Supplementary File). $F_c(T_\beta)$ is the TGF-β dependent collagen deposition rate. We normalized published experimental data [56, 57] and fitted the data to a Michaelis-Menten relationship to estimate the parameters $V_{T\beta}$ and $k_{T\beta}$ for the $F_c(T_\beta)$ formulation in Eq 7 (Fig S1B).

The TGF-β-dependent functions (Fig S1) for recruitment rate of fibroblasts ($F_g(T_\beta)$) and collagen deposition rate from fibroblasts ($F_c(T_\beta)$) were defined for TGF-β ranges of 0-10 ng/mL from experiments [56–58] and mathematical models [39, 42]. We calibrated the fibrosis model by adjusting the free parameters DS and MS to keep TGF-β concentration within the defined range (Fig S2). We iteratively changed DS while $MS = 0$ (turning off secretion from macrophages) and changed MS while $DS = 0$ (turning off secretion/activation from damaged sites) to estimate the concentration range of TGF-β (Fig S2); our goal was to keep TGF-β concentration within the range of experimental observations (0–10 ng/mL) where the TGF-β-dependent functions for fibroblasts were defined. We selected ranges of DS from 5×10^{-10} to 2×10^{-9} ng/min and MS from 5×10^{-10} to 5×10^{-9} ng/min (Table 2).

Code availability

The repository for version 5.0 of the overall model is available at `https://github.com/pc4covid19/pc4covid19/releases/tag/v5.0` [59]. We have provided the code and analysis files for the fibrosis model in a repository at `https://github.com/ashleefv/covid19fibrosis` [60].

Results and Discussion

We used the fibrosis model to predict the effects of stationary and mobile sources of TGF-β in fibroblast-mediated collagen deposition in the lung tissue in response to SARS-CoV-2 infection. The overall model produced predictions for the epithelial and infected cells, viral virions, and immune cells. The dynamics of these species are inputs to the fibrosis model. The fibrosis model output does not feedback to interact with any of the species of the overall model directly. A subset of the species not explicitly considered in the fibrosis model are shown in Fig S3. The fibrosis model was developed considering TGF-β activation from stationary agents to simulate the dynamics of TGF-β activation from latent stores in the ECM at the epithelial damage site. Also, TGF-β secretion from mobile sources simulated the contribution from M2 macrophages.

Table 3. Details for *in silico* experiment cases. Note that the values of parameters from Table 2 were used unless otherwise specified below.

Case	Description and parameter values	Illustrations
DM	Equal TGF-β activation rate from stationary damaged sites and secretion rate from mobile M2 macrophages: $DS = MS = 2 \times 10^{-9}$ ng/min	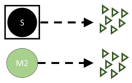
D	TGF-β activation only from stationary damaged sites: $DS = 2 \times 10^{-9}$ ng/min Secretion from mobile M2 macrophages is turned off: $MS = 0$ ng/min	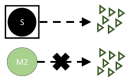
M	TGF-β activation from stationary damaged sites is turned off: $DS = 0$ ng/min Secretion only from mobile M2 macrophages: $MS = 2 \times 10^{-9}$ ng/min	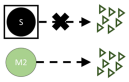
DHMH DLMH	TGF-β activation from stationary damaged sites is either high (DHMH): $DS = 2 \times 10^{-9}$ ng/min or low (DLMH): $DS = 5 \times 10^{-10}$ ng/min Secretion from mobile M2 macrophages is high: $MS = 5 \times 10^{-9}$ ng/min	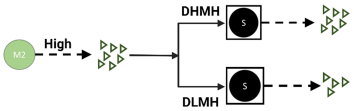
DHML DLML	TGF-β activation from stationary damaged sites is either high (DHML): $DS = 2 \times 10^{-9}$ ng/min or low (DLML): $DS = 5 \times 10^{-10}$ ng/min Secretion from mobile M2 macrophages is low: $MS = 5 \times 10^{-10}$ ng/min	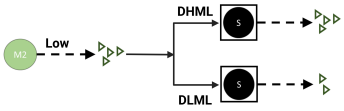
DA	Extension of case D with longer duration of TGF-β activation from stationary damaged sites by reducing secreting agents death rate by 100-fold: $AT = 1 \times 10^{-5}$ min^{-1}	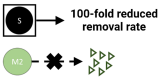
MA	Extension of case M with longer duration of TGF-β secretion from mobile M2 macrophages by setting fibroblast apoptosis rate to zero: $\mu_F = 0$ min^{-1}	
DAU	Extension of case DA with the uptake of TGF-β by fibroblasts: $U_F = 0.1$ min^{-1}	
MAU	Extension of case MA with the uptake of TGF-β by fibroblasts: $U_F = 0.1$ min^{-1}	

For our default case, we considered equal TGF-β activation and secretion rates from both sources (case DM, Table 3) within the physiological range of TGF-β. We analyzed the spatial behavior of both sources and compared them with independent experimental and clinical observations. We also conducted a series of *in silico* experiments by turning on/off TGF-β activation and secretion rates from stationary and mobile sources, increasing/decreasing the rates from sources in combination, increasing the duration of the sources, and including additional rules for removal of TGF-β by chemotaxing fibroblasts. We listed all the *in silico* experiments performed for this study in Table 3.

Spatial behaviors of TGF-β sources affect collagen dynamics

For the spatial behaviors, we considered the cases of DM, D, and M (Table 3). Figs S4 and S5 show the population spatial distributions over time for each agent type for these three cases. The stationary sources caused localized collagen deposition, whereas the distribution of collagen was more dispersed for mobile sources (Fig 2). We also observed two distinct peaks in TGF-β dynamics depending on the sources. Initially, the death of infected epithelial cells created secreting agents, which were stationary sources that activated latent TGF-β stored in the ECM at the damage sites. The number of these secreting agents fixed at damaged sites had a maximum around 5 days post-infection. The population reduced after that as the removal of the virions from the system occurred around 6 days (Fig S3A). As a result, we observed the first peak in TGF-β concentration around 5 days. The constant rate of activation and diffusion of TGF-β from stationary sources created localized fields with higher TGF-β concentrations. Active fibroblasts crowded at the sites of higher concentration of TGF-β and deposited collagen to cause localized distribution. In this model, M2 macrophages appear after the arrival of CD8+ T cells in the later phase of infection as we have encoded the rule that the interactions between M1 macrophages and CD8+ T cells transform M1 macrophages into the M2 phenotype, which acts as mobile sources of TGF-β. We observed the maximum number of macrophages around 9 days, which caused the second peak in the TGF-β profile. In the later phase of infection, damage was already present in the tissue when M2 macrophages arrived. M2 macrophages moved along the edge of damaged sites, phagocytosed dead and infected cells, cleared viral particles, and simultaneously secreted TGF-β. The movement of M2 macrophages along the edge of damaged sites caused higher concentrations of TGF-β at those sites. As a result, fibroblasts chemotaxed to those sites and deposited collagen. The deposited collagen was more dispersed with a higher collagen area fraction in the cases (DM and M) with mobile sources of TGF-β secretion compared to those (case D) with only stationary sources of TGF-β activation.

Case DM: equal TGF-β activation rate from stationary damaged sites and secretion rate from mobile macrophages

In case DM (Fig 2A and Fig S4), we observed localization of fibroblasts around 2 days (Fig S4B,I) due to the slow creation of new stationary sources before the inflammatory response infiltrated the tissue. Around 5 days (Fig S4C,J), the sudden increase of stationary sources and the appearance of mobile sources (Fig 2A) disrupted that localization. Fibroblasts started to move along the edge of damaged sites as the mobile sources moved along the edge to clear infected and dead cells that were more prominent from 9 days to 15 days (Fig S4F,G,M,N). Fibroblasts had partial localization between 5 days and 9 days (Fig S4C–F,J–M). But the locations of localization changed with the disappearance of stationary sources and the appearance of mobile sources.

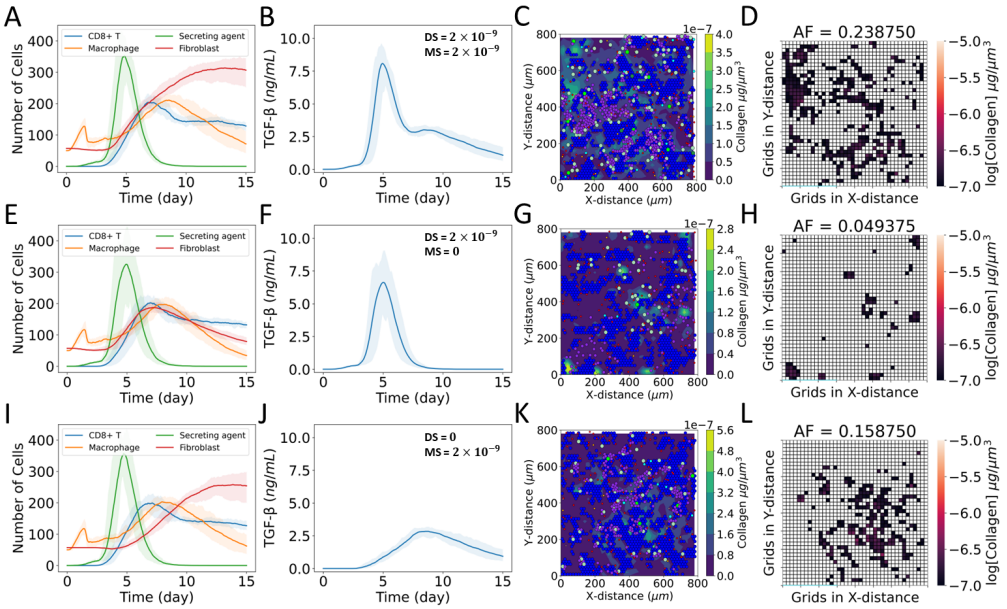

Fig 2. Effects of stationary and mobile sources of TGF-β on the dynamics of collagen deposition. (A–D) Case DM: equal TGF-β activation rate from stationary damaged sites and secretion rate from mobile macrophages, (E–H) Case D: TGF-β activation from stationary damaged sites only, and secretion from mobile macrophages is turned off, (I–L) Case M: TGF-β secretion from mobile macrophages only, and activation rate from stationary damaged sites is turned off. (A, E, I) Dynamics of populations of CD8+ T cells, macrophages, latent TGF-β activation sites (secreting agents), and fibroblasts; (B, F, J) dynamics of TGF-β concentration spatially averaged over the domain; (C, G, K) collagen deposition at damaged sites of tissue at day 15; (D, H, L) heat map showing collagen area fraction (AF) above the threshold value of 1×10^{-7} μg μm^{-3}. The solid curves represent the mean of predictions, and shaded areas represent the predictions between the 5th and 95th percentile of 15 replications of the agent-based model. The cases are defined in Table 3.

Case D: TGF-β activation from stationary damaged sites only

In case D (Fig 2E and Fig S5), as in case DM, the slow creation of new stationary sources resulted in fibroblast localization at damaged sites around 2 days (Fig S5B,I). The rapid creation of new sources disrupted the localization of fibroblasts around 5 days (Fig S5C,J). Localization of fibroblasts was again observed between 5 days and 9 days (Fig S5C–F,J–M) followed by delocalization of fibroblasts (Fig S5F,G,M,N) as stationary sources stopped secreting TGF-β (Fig 2F). The absence of TGF-β deactivated fibroblasts, halting fibroblast-mediated collagen deposition after 9 days (Fig S5F,G).

Case M: TGF-β secretion from mobile macrophages only

In case M (Fig 2I and Fig S6), we did not observe the localization of fibroblasts around 2 days (Fig S6B,I) when the TGF-β activation rate from damaged sites was turned off. Around 5 days (Fig S6C,J), fibroblasts were observed to move along the edge of damaged areas with the appearance of mobile sources of TGF-β (Fig 2I), which were more prominent from 9 days to 15 days. Overall the TGF-β concentrations for case M (Fig 2J) was less than that for cases DM (Fig 2B) and D (Fig 2F).

Comparison between simulated and clinical studies of collagen area fraction

In summary for cases DM, D, and M, we observed changes in fibrotic patterns depending on the partial creation and deletion of sources, mobility of the sources, and days post infection. The combination of stationary and mobile sources of TGF-β in different phases of infection created higher TGF-β concentration zones at more sites than a single source type, resulting in higher collagen area fractions (Fig 2D,H,L). The distribution of collagen area fractions for cases DM, D, and M are shown in the violin plots in Fig 3. The collagen area fraction was lower in case D, intermediate in case M and higher in case DM; Fig S7 shows the dynamics of the spatially averaged collagen concentrations for cases DM, D, and M. We observed exponential increases of spatially averaged collagen concentration in cases DM and M with a steeper slope in case DM; case D reached a plateau.

Literature values for measurements performed on postmortem transbronchial cryobiopsy samples of COVID-19 pneumonia diseased tissue were reported with 2%–38% collagen extension considering all the lobes of the lung [33]. Analogously to our simulation domain, the percentages of collagen in the samples were determined by restricting the samples to the alveolar tissue while excluding airway walls, vessels, and airspaces. Our simulated collagen area fractions (Fig 3) are in similar ranges (2%–40%) compared to the experimentally observed percentage of collagen extensions at the endpoint outcomes. Our simulated collagen area fractions are also in a similar range to the reported increase of collagen volume fraction in human lung with different stages of IPF [61] and predicted collagen area fractions over time in the multiscale model and experiments of MI [44]. Although the mechanisms for fibrosis may differ in these analyses, our findings suggest that the activity of TGF-β sources is an important aspect, which alone can generate fibrotic areas similar to experimental observations.

Higher TGF-β secretion rate from M2 macrophages leads to higher collagen area fraction

We explored the effects of varying the TGF-β activation rate from stationary damaged sites and the secretion rate from mobile macrophages at different levels in combination: cases DHMH, DLML, DHML, and DLMH (Table 3). Fig 4 shows the impacts of these variations, particularly on fibroblasts, TGF-β dynamics spatially averaged over the

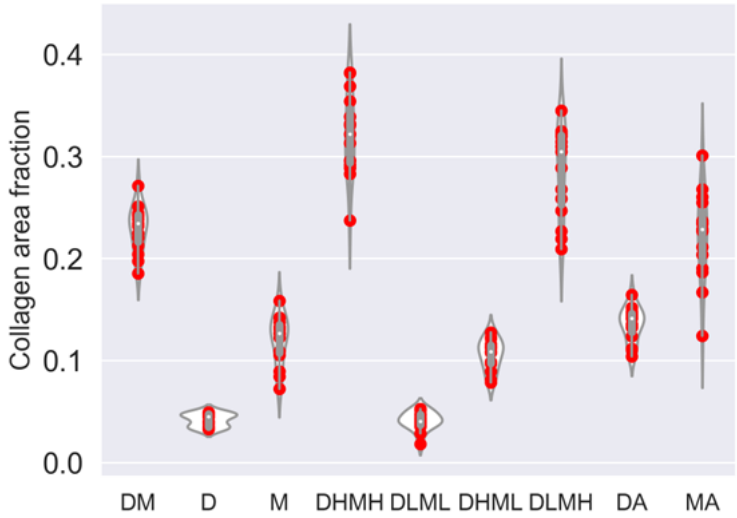

Fig 3. Quantification of collagen area fraction for different cases. Violin plots represent distribution, red solid circles represent data for 15 replications of each of the cases, and box plots show medians and quartiles. The cases listed along the x-axis are defined in Table 3.

domain, and the TGF-β impact on the distribution of collagen deposition. Figs S8–S11 show the population spatial distributions over time for each agent type for these four cases.

Cases DHMH and DLMH: TGF-β secretion from mobile macrophages is high and activation from stationary damaged sites is high/low

The agent dynamics showed high recruitment of fibroblasts for case DHMH (Fig 4A and Fig S8) and case DLMH (Fig 4M and Fig S11). We observed the highest collagen area fraction in case DHMH followed by case DLMH (Fig 3 and Fig 4D,P). In both cases, the TGF-β secretion rate from M2 macrophages was high. The spatially averaged TGF-β concentration remained high for the majority of the time period in both cases (Fig 4B,N) leading to very similar spatially averaged collagen concentrations (Fig 4C,O). Thus, mobile sources of TGF-β played a crucial role in higher collagen area fraction.

Cases DHML and DLML: TGF-β secretion from mobile macrophages is low and activation from stationary damaged sites is high/low

In both cases DHML and DLML when the TGF-β secretion rate from mobile sources was low, the collagen area fraction was reduced significantly (Fig 4H,L) compared with the previous two cases. We observed similar dynamics for case DHML (Fig 4I–L) as case D (Fig 2E–H). Despite differences in spatially averaged TGF-β concentration maxima between cases DHML and DLML (Fig 4F,J), their durations of TGF-β exposure were similar leading to very similar spatially averaged collagen concentrations (Fig 4G,K).

Comparison between simulated and experimental studies of fibroblasts dynamics

Experimental observations of mice models reported that during MI, fibroblasts appeared around day 4, and fibroblasts and collagen deposition remained prominent from day 4

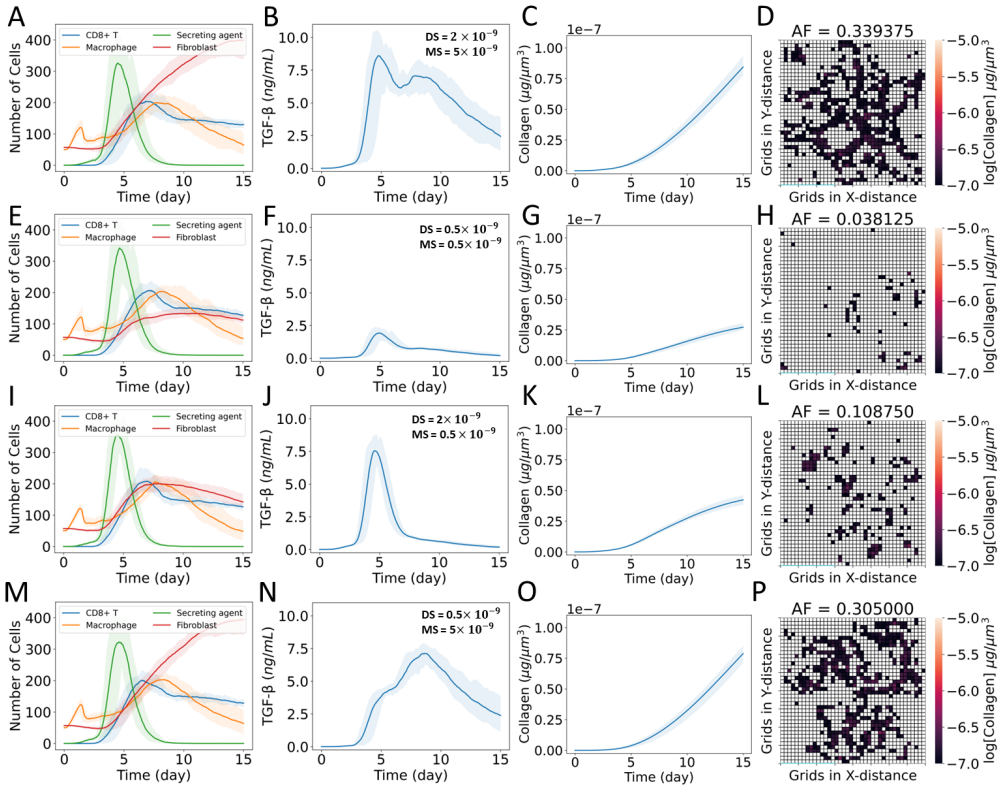

Fig 4. Effects of varying the TGF-β activation rate from stationary damaged sites DS and the secretion rate from mobile macrophages MS at different levels in combination. H and L denote higher and lower values, respectively, of DS when they come after D and of MS when they come after M in the case names. (A–D) Case DHMH, (E–H) case DLML, (I–L) case DHML, and (M-P) case DLMH. (A, E, I, M) Dynamics of populations of CD8+ T cells, macrophages, latent TGF-β activation sites (secreting agents), and fibroblasts; (B, F, J, N) dynamics of TGF-β concentration spatially averaged over the domain; (C, G, K, O) dynamics of collagen concentration spatially averaged over the domain; and (D, H, L, P) heat map showing collagen area fraction (AF) above the threshold value of 1×10^{-7} μg μm^{-3}. The solid curves represent the mean of predictions, and shaded areas represent the predictions between the 5th and 95th percentile of 15 replications of the agent-based model. The cases are defined in Table 3.

to 21 [52]. We also observed the activation and recruitment of fibroblasts around 4 days (Fig 4), and fibroblast population and collagen deposition remained prominent for a higher secretion rate of TGF-β from M2 macrophages (Fig 4A in case DHMH and Fig 4M in case DLMH). Other data have been published showing the relative abundance of fibroblasts was higher than macrophages in COVID-19 patients [62], which was also observed in the simulation cases we considered. The intercellular model for fibrosis during MI also reported similar dynamics of macrophages, fibroblasts, latent TGF-β, and collagen [43] to some of our simulation cases. However, that model focused on fibrosis in a different organ, so exact agreement was not expected.

Longer duration of stationary TGF-β sources causes localized fibrotic pattern

We explored the impact of longer duration for both stationary and mobile sources on fibrotic outcomes: cases DA and MA (Table 3).

Case DA: longer duration of TGF-β activation from stationary sources

Latent stores TGF-β from damaged sites may continue to be activated for a longer duration for severe lung tissue damage. The effects of the longer duration of stationary sources (case DA) are shown in Fig 5A–D. In this case, we turned off the secretion from mobile sources ($MS = 0$) to observe the response from damaged sites alone. We increased the released TGF-β activation duration 100-fold by decreasing the secreting agent death rate (AT) by a factor of 100. Fig 5A shows a greater accumulation of secreting agents over time. The concentration profile of TGF-β is proportional to the number of secreting agent. The TGF-β concentration has an approximately 2-fold larger maximum value compared to all previous cases with a peak value at an earlier phase of infection (Fig 5B). The spatial profile showed localized collagen fields with high concentrations of deposited collagen (Fig 5D). However, the violin plot of the collagen area fraction in Fig 3 showed results higher than case D and intermediate collagen area fraction compared to other cases. Therefore, even with a lower collagen fraction, localized damage with high collagen deposition can lead to long-term fibrosis by the dysregulation in the duration of activation from spatially-localized latent TGF-β sources.

We observed localization of fibroblasts around 2 days with slow creation of stationary sources (Fig S12B,I), which is disrupted around 5 days (Fig S12C,J) by the rapid creation of new stationary sources. The longer duration of stationary sources resulted in persistent localization of fibroblasts at the damaged sites from 5 days to 15 days (Fig S12C–G,I–N). The localization pattern remained the same during that period due to a slow decrease of stationary sources. The number of accumulated fibroblasts also increased in localized positions.

As a further *in silico* experiment, we changed the initial placement of virions in case DA. All cases thus far used uniform random distribution of virions. In this scenario, we considered a Gaussian distribution at the tissue center for case DA. Figs S13 and S14 showed higher fibroblast accumulation and denser collagen deposition near the center compared with the default random distribution. While only a single major fibrotic region developed (Fig S14D), the collagen concentration was the highest among all cases considered here. Thus, fibrotic patterns vary depending on the location of initial infection sites.

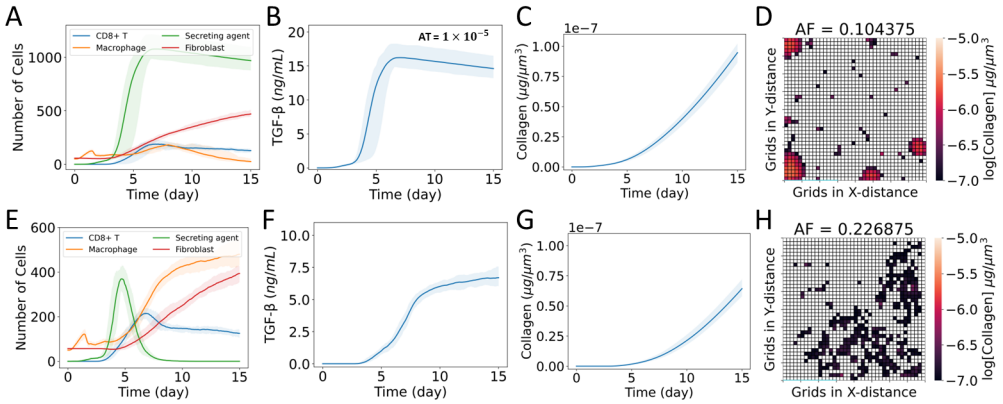

Fig 5. Effects of longer duration of stationary and mobile sources of TGF-β. (A–D) Case DA: longer duration of stationary damaged site sources and (E–H) case MA: longer duration of mobile macrophage sources. (A, E) Dynamics of populations of CD8+ T cells, macrophages, latent TGF-β activation sites (secreting agents), and fibroblasts; (B, F) dynamics of TGF-β concentration spatially averaged over the domain; (C, G) dynamics of collagen concentration spatially averaged over the domain; and (D, H) heat map showing collagen area fraction (AF) above the threshold value of 1×10^{-7} μg μm^{-3}. The solid curves represent the mean of predictions, and shaded areas represent the predictions between the 5th and 95th percentile of 15 replications of the agent-based model. The cases are defined in Table 3.

Case MA: no apoptosis of M2 macrophages

Sefik et al. [63] reported experimental results showing that severe SARS-CoV-2 infection increases human lung macrophage numbers at 4 days with a peak value at 14 days, and the number of macrophages remains high until 28 days. They also observed similar dynamics for the number of macrophages marked by CD206hi (a marker for M2 macrophages [64]), CD86+, and CD169+ expression. Sefik et al. [63] further reported persistent lung tissue pathology in the exudative, organizing, and fibrotic phases, with changes in affected tissue areas between 45% and 55% from uninfected tissue. We investigated whether the model could predict these findings by considering a similar scenario (case MA) by turning off the apoptosis rate of M2 macrophages ($\mu_F = 0$) and the activation rate of TGF-β from damaged sites ($DS = 0$ ng/min). In Fig 5E–H, we showed the effects of longer activation of M2 macrophages. The spatially averaged collagen concentration (Fig 5G) had a similar shape, but somewhat smaller values, than that for case DA (Fig 5C), We observed a higher number of macrophages in case MA compared to other cases (Fig 5E and Fig S15). To determine the compositions of the macrophage populations reported in Figs 2 and 5, we generated Fig S16; in all four cases shown (as in the others not shown), the M2 macrophage phenotype dominates the total macrophage population as the numbers of secreting agents peak (due to death of infected epithelial cells). The simulated dynamics of M2 macrophages in case MA (Fig S16) were also similar to experimental observations of Sefik et al. [63]. In Fig 5F, the spatially averaged TGF-β concentration increased over time, remained high, and shifted its peak value compared to case DA. We also observed a higher collagen area fraction in case MA than in cases M and DA (Fig 3). The persistent presence of M2 macrophages caused a higher amount of collagen deposition, higher collagen area fraction, and localization of fibroblasts from 9 days to 15 days (Fig S15).

Partial removal of TGF-β changes fibrotic pattern

We considered the impact of TGF-β uptake by fibroblasts as they chemotax through the domain by adding an uptake term in Eq 1:

$$\frac{\partial T_\beta}{\partial t} = D_{T\beta}\nabla^2 T_\beta - \mu_{T\beta} T_\beta + \sum_{cells\ i} \delta(x - x_i)(E_{T\beta,i} - U_{F,i} F_{V,i} T_\beta) \tag{8}$$

where $U_{F,i}$ is the uptake rate of TGF-β by fibroblast cell i and $F_{V,i}$ is the volume of fibroblast cell i. The uptake rate of TGF-β by fibroblasts was assumed equivalent to the uptake rate of debris in the overall model. Here we considered cases DAU and MAU (Table 3). Figs S17 and S18 show the population spatial distributions over time for each agent type for these two cases. Fig S19 compares the collagen area fractions for these final cases to other cases.

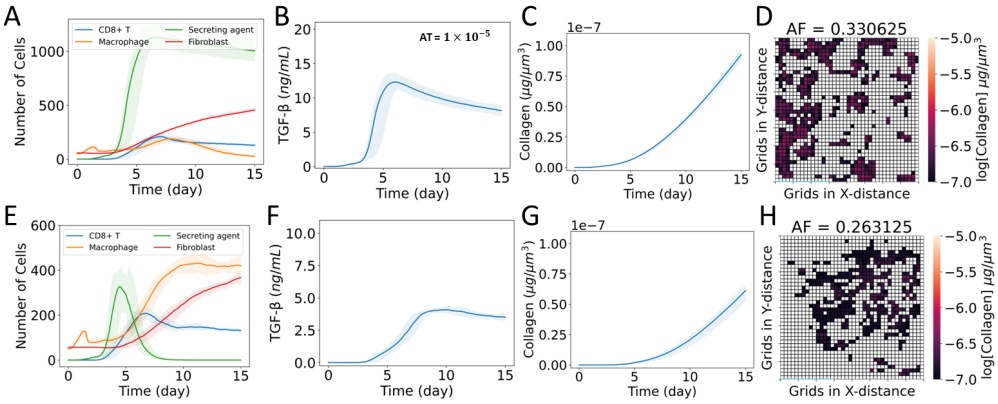

Fig 6. Effects of the uptake of TGF-β by fibroblasts. (A–D) Case DAU: uptake of TGF-β by fibroblasts in case DA and (E–H) case MAU: uptake of TGF-β by fibroblasts in case MA. (A, E) Dynamics of populations of CD8+ T cells, macrophages, latent TGF-β activation sites (secreting agents), and fibroblasts; (B, F) dynamics of TGF-β concentration spatially averaged over the domain; (C, G) dynamics of collagen concentration spatially averaged over the domain; and (D, H) heat map showing collagen area fraction (AF) above the threshold value of 1×10^{-7} μg μm^{-3}. The solid curves represent the mean of predictions, and shaded areas represent the predictions between the 5th and 95th percentile of 15 replications of the agent-based model. The cases are defined in Table 3.

Case DAU: uptake of TGF-β by fibroblasts in case DA

We considered the uptake of TGF-β in case DA and termed this scenario as case DAU. Although the population dynamics and mean collagen concentrations (Fig 6A,C) remained similar to those in case DA (Fig 5A,C), we observed variations in the spatially averaged TGF-β dynamics with a reduced peak value (Fig 6B). The uptake of TGF-β also changed the concentration gradient of TGF-β in the ECM (Eq 3), which caused delocalization and redistribution of fibroblasts in other tissue areas (Fig S17). This effectively maintained a chemotactic gradient to drive fibroblast movement. As a result, we observed a significantly higher collagen area fraction in case DAU compared to cases D and DA (Fig 6D and S19).

Case MAU: uptake of TGF-β by fibroblasts in case MA

We also considered the uptake of TGF-β in case MA and termed that scenario case MAU. Here, we observed reductions in spatially averaged TGF-β dynamics with similar populations and spatially averaged collagen dynamics (Fig 6E–H) compared to case MA (Fig 5E–H). Although the delocalization and redistribution of fibroblasts were observed in case MAU (Fig S18), collagen area fractions remained similar to case MA (Fig S19). We also observed higher collagen area fractions in case DAU compared to case MAU. Our findings suggest that removing TGF-β from ECM when persistent latent TGF-β activation sites are present can spread fibrotic areas in tissue, which is particularly noticeable when spatially averaged TGF-β concentration is high.

Potential future application to clinical trials

Our results give critical insight into the current clinical trials targeting TGF-β for lung fibrosis. At present, two of the promising anti-TGF-β drugs for lung fibrosis are pirfenidone and PLN-74809, and both are in Phase II clinical trials [65]. The mechanism of pirfenidone involves inhibiting the activity of TGF-β by stopping the maturation of latent TGF-β [66,67]. The drug PLN-74809 inhibits $\alpha v\beta_6$ and $\alpha v\beta_1$ integrins to prevent the activation of latent TGF-β [68]. In our simulations, we observed (1) changing the TGF-β sources alters the fibrotic pattern and (2) removing TGF-β from the ECM in the presence of persistent activation sizes leads to increases in the collagen area fractions. If these computational findings can be validated, the results have important implications for ongoing clinical trials: improving the trial outcomes requires a more thorough consideration of the spatial behavior of fibroblasts and immune cells and the rate and duration of TGF-β activation. Partial removal of TGF-β from ECM or inhibition of TGF-β activation from sources may change the chemotactic direction of fibroblasts and lead to fibrotic areas with higher collagen area fraction. It is essential to consider the spatial behavior and activity of sources before targeting them for inhibition of TGF-β as fibrosis is a spatial phenomenon.

Conclusions

The multiscale tissue simulator (overall model and fibrosis model) described here gives insight into the dynamics and impact of TGF-β sources in fibroblast-mediated collagen deposition at damaged sites of SARS-CoV-2 infected tissue in COVID-19. We applied this model to investigate the spatial behaviors of sources of TGF-β, the activation rate of TGF-β, and the activation duration of TGF-β sources in the process of lung fibrosis. Fibrosis is a spatial event; thus, it is essential to consider the spatial properties of the sources of the key biomarkers observed during the process. Our results showed localized collagen deposition from stationary sources of TGF-β and dispersed collagen deposition from mobile sources of TGF-β. Our results indicated that M2 macrophages and their persistent presence were mainly responsible for higher collagen area fractions. The computational observations were supported by independent experimental and clinical observations. We predicted a longer duration of stationary TGF-β sources could lead to fibrosis even with a lower collagen area fraction. Also, partial removal of TGF-β from ECM changed the chemotactic gradient of fibroblasts, resulting in a higher collagen area fraction. In the future, the accuracy of the predictions could further be improved by considering the premorbidity of patient groups (e.g., hypertension), different phenotypes of fibroblasts (e.g., myofibroblasts), negative regulators for collagen degradation (e.g., MMP9), and collagen feedback to epithelial cells for regrowth and wound healing and to immune cells for transport properties through the evolving ECM. The quantification of the collagen deposition dynamics depending on the activity of sources may benefit

treatment strategies controlling TGF-β and help characterize the evolution of fibrosis in COVID-19 survivors.

Supporting information

Supplementary File The Supplementary File contains supporting information and figures organized into the following sections: TGF-β-dependent functions for fibroblasts (Fig S1); fibroblast collagen production rate k_{FC}; effects of TGF-β activation/secretion rate from each source (Fig S2); dynamics of virions, neutrophils, dendritic cells, and CD4 cells (Fig S3); effects of turning on/off TGF-β activation and secretion rates from stationary and mobile sources (Figs S4–S7); effects of varying the TGF-β activation rate from stationary damaged sites and the secretion rate from mobile macrophages at different levels in combination (Figs S8–S11); effects of increasing the duration of the sources (Figs S12–S16); and effects of uptake of TGF-β (Figs S17–S19).

Acknowledgments

This work was supported by the National Institutes of Health grant R35GM133763 (to A.N.F.V.), the University at Buffalo, and the Center for Computational Research at the University at Buffalo. We thank the scientific community for fibrosis model feedback, particularly Amber M. Smith, Thomas Hillen, and Yafei Wang.

References

1. Michalski JE, Kurche JS, Schwartz DA. From ARDS to pulmonary fibrosis: the next phase of the COVID-19 pandemic? Translational Research. 2022;241:13–24.
2. Li X, Shen C, Wang L, Majumder S, Zhang D, Deen MJ, et al. Pulmonary fibrosis and its related factors in discharged patients with new corona virus pneumonia: a cohort study. Respiratory Research. 2021;22(1):1–11.
3. Rai DK, Sharma P, Kumar R. Post covid 19 pulmonary fibrosis. Is it real threat? Indian Journal of Tuberculosis. 2021;68(3):330–333.
4. Meduri GU, Eltorky MA. Understanding ARDS-associated fibroproliferation. Intensive Care Medicine. 2015;41(3):517–520.
5. Jacobs JJ. Persistent SARS-2 infections contribute to long COVID-19. Medical Hypotheses. 2021;149:110538.
6. Tonelli R, Marchioni A, Tabbì L, Fantini R, Busani S, Castaniere I, et al. Spontaneous breathing and evolving phenotypes of lung damage in patients with COVID-19: review of current evidence and forecast of a new scenario. Journal of Clinical Medicine. 2021;10(5):975.
7. Nalbandian A, Sehgal K, Gupta A, Madhavan MV, McGroder C, Stevens JS, et al. Post-acute COVID-19 syndrome. Nature Medicine. 2021;27(4):601–615.
8. Ryan FJ, Hope CM, Masavuli MG, Lynn MA, Mekonnen ZA, Yeow AEL, et al. Long-term perturbation of the peripheral immune system months after SARS-CoV-2 infection. BMC Medicine. 2022;20(1):1–23.

9. John AE, Joseph C, Jenkins G, Tatler AL. COVID-19 and pulmonary fibrosis: A potential role for lung epithelial cells and fibroblasts. Immunological Reviews. 2021;302(1):228–240.

10. Yim J, Lim HH, Kwon Y. COVID-19 and pulmonary fibrosis: therapeutics in clinical trials, repurposing, and potential development. Archives of Pharmacal Research. 2021;44(5):499–513.

11. Zou JN, Sun L, Wang BR, Zou Y, Xu S, Ding YJ, et al. The characteristics and evolution of pulmonary fibrosis in COVID-19 patients as assessed by AI-assisted chest HRCT. PloS One. 2021;16(3):e0248957.

12. Han X, Fan Y, Alwalid O, Li N, Jia X, Yuan M, et al. Six-month follow-up chest CT findings after severe COVID-19 pneumonia. Radiology. 2021;299(1):E177–E186.

13. Matthay MA, Zemans RL, Zimmerman GA, Arabi YM, Beitler JR, Mercat A, et al. Acute respiratory distress syndrome. Nature Reviews Disease Primers. 2019;5(1):1–22.

14. Huang X, Xiu H, Zhang S, Zhang G. The role of macrophages in the pathogenesis of ALI/ARDS. Mediators of Inflammation. 2018;2018.

15. Bösmüller H, Matter M, Fend F, Tzankov A. The pulmonary pathology of COVID-19. Virchows Archiv. 2021;478(1):137–150.

16. Wendisch D, Dietrich O, Mari T, von Stillfried S, Ibarra IL, Mittermaier M, et al. SARS-CoV-2 infection triggers profibrotic macrophage responses and lung fibrosis. Cell. 2021;184(26):6243–6261.

17. Frangogiannis N. Transforming growth factor-β in tissue fibrosis. Journal of Experimental Medicine. 2020;217(3):e20190103.

18. Sheppard D. Transforming growth factor β: a central modulator of pulmonary and airway inflammation and fibrosis. Proceedings of the American Thoracic Society. 2006;3(5):413–417.

19. Sakai N, Tager AM. Fibrosis of two: Epithelial cell-fibroblast interactions in pulmonary fibrosis. Biochimica et Biophysica Acta (BBA)-Molecular Basis of Disease. 2013;1832(7):911–921.

20. Saito A, Horie M, Nagase T. TGF-β signaling in lung health and disease. International Journal of Molecular Sciences. 2018;19(8):2460.

21. Lodyga M, Hinz B. TGF-β1 - A truly transforming growth factor in fibrosis and immunity. Seminars in Cell & Developmental Biology. 2020;101:123–139.

22. Yue X, Shan B, A Lasky J. TGF-β: titan of lung fibrogenesis. Current Enzyme Inhibition. 2010;6(2):67–77.

23. Nacu N, Luzina IG, Highsmith K, Lockatell V, Pochetuhen K, Cooper ZA, et al. Macrophages produce TGF-β-induced (β-ig-h3) following ingestion of apoptotic cells and regulate MMP14 levels and collagen turnover in fibroblasts. Journal of Immunology. 2008;180(7):5036–5044.

24. Kelly A, Gunaltay S, McEntee CP, Shuttleworth EE, Smedley C, Houston SA, et al. Human monocytes and macrophages regulate immune tolerance via integrin αvβ8-mediated TGFβ activation. Journal of Experimental Medicine. 2018;215(11):2725–2736.

25. Qin Y, Garrison BS, Ma W, Wang R, Jiang A, Li J, et al. A milieu molecule for TGF-β required for microglia function in the nervous system. Cell. 2018;174(1):156–171.

26. Bonniaud P, Margetts PJ, Kolb M, Schroeder JA, Kapoun AM, Damm D, et al. Progressive transforming growth factor β1–induced lung fibrosis is blocked by an orally active ALK5 kinase inhibitor. American Journal of Respiratory and Critical Care Medicine. 2005;171(8):889–898.

27. Ferreira-Gomes M, Kruglov A, Durek P, Heinrich F, Tizian C, Heinz GA, et al. SARS-CoV-2 in severe COVID-19 induces a TGF-β-dominated chronic immune response that does not target itself. Nature Communications. 2021;12(1):1–14.

28. Vaz de Paula CB, Nagashima S, Liberalesso V, Collete M, da Silva FPG, Oricil AGG, et al. COVID-19: immunohistochemical analysis of TGF-β signaling pathways in pulmonary fibrosis. International Journal of Molecular Sciences. 2021;23(1):168.

29. Barron L, Gharib SA, Duffield JS. Lung pericytes and resident fibroblasts: busy multitaskers. American Journal of Pathology. 2016;186(10):2519–2531.

30. Vaz de Paula CB, Nagashima S, Liberalesso V, Collete M, da Silva FPG, Oricil AGG, et al. COVID-19: Immunohistochemical Analysis of TGF-β Signaling Pathways in Pulmonary Fibrosis. International Journal of Molecular Sciences. 2022;23(1):168.

31. DeLeon-Pennell KY, Barker TH, Lindsey ML. Fibroblasts: the arbiters of extracellular matrix remodeling. Matrix Biology. 2020;91:1–7.

32. Good RB, Eley JD, Gower E, Butt G, Blanchard AD, Fisher AJ, et al. A high content, phenotypic 'scar-in-a-jar' assay for rapid quantification of collagen fibrillogenesis using disease-derived pulmonary fibroblasts. BMC Biomedical Engineering. 2019;1(1):1–10.

33. Ball L, Barisione E, Mastracci L, Campora M, Costa D, Robba C, et al. Extension of Collagen Deposition in COVID-19 Post Mortem Lung Samples and Computed Tomography Analysis Findings. International Journal of Molecular Sciences. 2021;22(14):7498.

34. B Moore B, Lawson WE, Oury TD, Sisson TH, Raghavendran K, Hogaboam CM. Animal models of fibrotic lung disease. American Journal of Respiratory Cell and Molecular Biology. 2013;49(2):167–179.

35. Li Xh, Fang Zn, Guan Tm, Lin Jj, Sun Ch, Huang Sy, et al. A novel collagen area fraction index to quantitatively assess bowel fibrosis in patients with Crohn's disease. BMC Gastroenterology. 2019;19(1):1–7.

36. Brown BN, Price IM, Toapanta FR, DeAlmeida DR, Wiley CA, Ross TM, et al. An agent-based model of inflammation and fibrosis following particulate exposure in the lung. Mathematical Biosciences. 2011;231(2):186–196.

37. Warsinske HC, Wheaton AK, Kim KK, Linderman JJ, Moore BB, Kirschner DE. Computational modeling predicts simultaneous targeting of fibroblasts and epithelial cells is necessary for treatment of pulmonary fibrosis. Frontiers in Pharmacology. 2016;7:183.

38. Cogno N, Bauer R, Durante M. A 3D Agent-Based Model of Lung Fibrosis. Symmetry. 2022;14(1):90.

39. Ceresa M, Olivares AL, Noailly J, González Ballester MA. Coupled immunological and biomechanical model of emphysema progression. Frontiers in Physiology. 2018;9:388.

40. Hao W, Marsh C, Friedman A. A mathematical model of idiopathic pulmonary fibrosis. PLoS One. 2015;10(9):e0135097.

41. Murtha LA, Schuliga MJ, Mabotuwana NS, Hardy SA, Waters DW, Burgess JK, et al. The Processes and Mechanisms of Cardiac and Pulmonary Fibrosis. Frontiers in Physiology. 2017;8:777.

42. Jin YF, Han HC, Berger J, Dai Q, Lindsey ML. Combining experimental and mathematical modeling to reveal mechanisms of macrophage-dependent left ventricular remodeling. BMC Systems Biology. 2011;5(1):1–14.

43. Chowkwale M, Lindsey ML, Saucerman JJ. Intercellular model predicts mechanisms of inflammation-fibrosis coupling after myocardial infarction. The Journal of Physiology. 2022;.

44. Rikard SM, Athey TL, Nelson AR, Christiansen SL, Lee JJ, Holmes JW, et al. Multiscale coupling of an agent-based model of tissue fibrosis and a logic-based model of intracellular signaling. Frontiers in Physiology. 2019; p. 1481.

45. Getz M, Wang Y, An G, Becker A, Cockrell C, Collier N, et al. Iterative community-driven development of a SARS-CoV-2 tissue simulator. BioRxiv preprint. 2021;DOI: 10.1101/2020.04.02.019075v5.

46. Ghaffarizadeh A, Heiland R, Friedman SH, Mumenthaler SM, Macklin P. PhysiCell: An open source physics-based cell simulator for 3-D multicellular systems. PLoS Computational Biology. 2018;14(2):e1005991.

47. Pienaar E, Cilfone NA, Lin PL, Dartois V, Mattila JT, Butler JR, et al. A computational tool integrating host immunity with antibiotic dynamics to study tuberculosis treatment. Journal of Theoretical Biology. 2015;367:166–179.

48. Jenner AL, Aogo RA, Alfonso S, Crowe V, Deng X, Smith AP, et al. COVID-19 virtual patient cohort suggests immune mechanisms driving disease outcomes. PLoS Pathogens. 2021;17(7):e1009753.

49. Getz M, Wang Y, An G, Becker A, Cockrell C, Collier N, et al. Rapid community-driven development of a SARS-CoV-2 tissue simulator. BioRxiv preprint. 2020;DOI: 10.1101/2020.04.02.019075v3.

50. Ghaffarizadeh A, Friedman SH, Macklin P. BioFVM: an efficient, parallelized diffusive transport solver for 3-D biological simulations. Bioinformatics. 2016;32(8):1256–1258.

51. SourceForge. Plot Digitizer. (Online; accessed 21-October-2021), `http://plotdigitizersourceforgenet/`. 2015;.

52. Yang F, Liu YH, Yang XP, Xu J, Kapke A, Carretero OA. Myocardial infarction and cardiac remodelling in mice. Experimental Physiology. 2002;87(5):547–555.

53. Padovan-Merhar O, Nair GP, Biaesch AG, Mayer A, Scarfone S, Foley SW, et al. Single mammalian cells compensate for differences in cellular volume and DNA copy number through independent global transcriptional mechanisms. Molecular Cell. 2015;58(2):339–352.

54. Lamond AI, Sleeman JE. Nuclear substructure and dynamics. Current Biology. 2003;13(21):R825–R828.

55. Trepat X, Chen Z, Jacobson K. Cell migration. Comprehensive Physiology. 2012;2(4):2369.

56. Roberts AB, Sporn MB, Assoian RK, Smith JM, Roche NS, Wakefield LM, et al. Transforming growth factor type beta: rapid induction of fibrosis and angiogenesis in vivo and stimulation of collagen formation in vitro. Proceedings of the National Academy of Sciences. 1986;83(12):4167–4171.

57. Ignotz RA, Massague J. Transforming growth factor-beta stimulates the expression of fibronectin and collagen and their incorporation into the extracellular matrix. Journal of Biological Chemistry. 1986;261(9):4337–4345.

58. Wahl SM, Hunt DA, Wakefield LM, McCartney-Francis N, Wahl LM, Roberts AB, et al. Transforming growth factor type beta induces monocyte chemotaxis and growth factor production. Proceedings of the National Academy of Sciences. 1987;84(16):5788–5792.

59. Heiland R, Macklin P. pc4covid19; 2022.

60. Islam MA, Ford Versypt AN. covid19fibrosis; 2022.

61. McDonough JE, Ahangari F, Li Q, Jain S, Verleden SE, Herazo-Maya J, et al. Transcriptional regulatory model of fibrosis progression in the human lung. JCI Insight. 2019;4(22).

62. Delorey TM, Ziegler CG, Heimberg G, Normand R, Yang Y, Segerstolpe Å, et al. COVID-19 tissue atlases reveal SARS-CoV-2 pathology and cellular targets. Nature. 2021;595(7865):107–113.

63. Sefik E, Israelow B, Mirza H, Zhao J, Qu R, Kaffe E, et al. A humanized mouse model of chronic COVID-19. Nature Biotechnology. 2022;40(6):906–920.

64. Tedesco S, Bolego C, Toniolo A, Nassi A, Fadini GP, Locati M, et al. Phenotypic activation and pharmacological outcomes of spontaneously differentiated human monocyte-derived macrophages. Immunobiology. 2015;220(5):545–554.

65. Shi N, Wang Z, Zhu H, Liu W, Zhao M, Jiang X, et al. Research progress on drugs targeting the TGF-β signaling pathway in fibrotic diseases. Immunologic Research. 2022; p. 1–13.

66. Hamidi SH, Kadamboor Veethil S, Hamidi SH. Role of pirfenidone in TGF-β pathways and other inflammatory pathways in acute respiratory syndrome coronavirus 2 (SARS-CoV-2) infection: a theoretical perspective. Pharmacological Reports. 2021;73(3):712–727.

67. Sathiyamoorthy G, Sehgal S, Ashton RW. Pirfenidone and nintedanib for treatment of idiopathic pulmonary fibrosis. Southern Medical Journal. 2017;110(6):393–398.

68. Cosgrove G, Decaris M, Wong S, Park E, Turner S, Adegbite E, et al. PLN-74809, an oral, dual-selective αvβ6/αvβ1 inhibitor in Phase 2 clinical trials for idiopathic pulmonary fibrosis (IPF), sustainably reduces transforming growth factor beta (TGF-β) activity in the lungs of healthy participants with once-daily dosing. In: D30. The Injured Lung: Mechanisms and Therapeutic Targets. American Thoracic Society; 2022. p. A5251–A5251.